Intrinsically Dominant Conformational Diversity in PDZ1 within the Tandem PDZ1-PDZ2 of Human Syntenin-1 Underlined by Crystal Structures.

Natsuno Ando[1], Yuya Hanazono[2], Koya Sakuma[3], Nobutaka Numoto[2,4], Takeshi Tenno[1,5], Atsunori Oshima[3,6,7], Nobutoshi Ito[2] and Hidekazu Hiroaki[1,5,7,] *.

[1] Graduate School of Pharmaceutical Sciences, Nagoya University, Furocho, Chikusa, Nagoya, Aichi, Japan

[2] Laboratory of Structural Biology, Medical Research Institute, Institute of Science Tokyo, 1-5-45, Yushima Bunkyo-ku, Tokyo, Japan

[3] Cellular and Structural Physiology Institute (CeSPi), Nagoya University, Furocho, Chikusa, Nagoya, Aichi, Japan

[4] International Center for Structural Biology, Research Institute for Interdisciplinary Science, Okayama University, Tsushima Naka 3-1-1, Kita, Okayama 700-8530, Japan.

[5] BeCellBar, LLC., Furocho, Chikusa, Nagoya, Aichi, Japan.

[6] Institute for Glyco-core Research (iGCORE), Tokai National Higher Education and Research System, Furocho, Chikusa, Nagoya, Aichi, Japan [正式名称?]

[7] Center for One Medicine Innovative Translational Research; COMIT, Nagoya University, Nagoya, Aichi, Japan

*** Correspondence:**

Hidekazu Hiroaki*

hiroaki.hidekazu.j7@f.mail.nagoya-u.ac.jp

Keywords

Syntenin-1, Tandem PDZ domains, Conformational diversity, Structural plasticity, X-ray crystallography, Molecular Dynamics Simulation, Protein-Protein Interactions,

Abstract

The intrinsic dynamic asymmetry between homologous PDZ domains in multidomain scaffold proteins offers critical insights into evolutionary mechanisms enabling multivalent partner recognition. Through systematic X-ray crystallographic analysis of human syntenin-1's PDZ1-PDZ2 tandem, we resolve nine high-resolution structures that uncover fundamental differences in conformational plasticity between these sequentially similar domains. Pairwise root-mean-squared deviation (RMSD) analysis of 20 PDZ1 structures across multiple crystal forms reveals substantial structural variability concentrated in the Lys119-Ile125 and Ala181-Glu184 loops - key regions governing ligand specificity within PDZ1's binding cleft. In stark contrast, PDZ2 maintains remarkable structural conservation across all crystallographic environments, indicating divergent evolutionary constraints on these tandem domains. Crucially, comparative analysis of isotropic B-factors demonstrates their inadequacy in capturing the full scope of conformational heterogeneity, emphasizing the necessity of multi-structure comparisons for mapping dynamic landscapes.

Molecular dynamics (MD) simulations implemented through GROMACS corroborate these crystallographic observations, showing elevated residue-specific fluctuation (RMSF) values in PDZ1's ligand-binding interface compared to analogous PDZ2 regions. This consistency across experimental and computational approaches confirms that PDZ1's conformational diversity represents an inherent biophysical property rather than crystallographic artifact. The observed dynamic asymmetry suggests a functional division of labor: PDZ1's structural plasticity enables broad ligand recognition via conformational selection mechanisms, while PDZ2's rigid architecture likely stabilizes the tandem domain arrangement. These findings provide an atomic-level rationale for syntenin-1's pleiotropic roles in cellular signaling and establish a structural

blueprint for developing domain-selective therapeutics. Given syntenin-1's clinical relevance in cancer metastasis, viral pathogenesis, and neurodevelopmental disorders, our work advances strategies for selectively modulating PDZ1-mediated interactions while preserving PDZ2's scaffolding functions through structure-guided inhibitor design. (258 words)

Highlights

- ✧ Crystal structures of human Syntenin-1's PDZ1-PDZ2 tandem reveal intrinsic conformational plasticity in PDZ1, particularly in ligand-binding loops, contrasting with PDZ2's rigid architecture
- ✧ Pairwise RMSD analysis of 20 PDZ1 structures demonstrates substantial structural variability in the Lys119-Ile125 and Ala181-Glu184 loops, key regions governing ligand specificity
- ✧ Molecular dynamics simulations confirm that PDZ1's conformational diversity is an inherent biophysical property, not a crystallographic artifact
- ✧ The asymmetric dynamics between PDZ1 and PDZ2 suggest a functional division: PDZ1's plasticity enables broad ligand recognition while PDZ2 stabilizes the tandem arrangement
- ✧ These findings provide a structural basis for developing domain-selective Syntenin-1 inhibitors with potential applications in cancer metastasis, viral pathogenesis, and neurodevelopmental disorders

Introduction

Syntenin-1 (SDCBP/MDA-9) is a 32 kDa cytosolic scaffold protein that serves as either an adaptor or a critical hub in cellular signaling and trafficking networks [Grootjans, J. J., et al., 1997]. The architecture of syntenin-1 features two (Postsynaptic density-95/Discs large/Zonula occludens-1 (PDZ) domains in tandem (PDZ1 and PDZ2) flanked by N- and C-terminal regions, enabling it to act as a versatile protein-protein interaction hub. While syntenin-1 is extensively studied in context of its role in exosome biogenesis through interactions with syndecans and ALIX [Baietti, M. F., et al., 2012], emerging evidence highlights its other broader functions, including synaptic regulation [Hirbec, H., et al., 2005], cytoskeletal dynamics [Zimmermann, P., et al.,

2001], receptor trafficking [Zimmermann, P., et al., 2005], and viral entry [Gordon-Alonso, M., et al., 2012]. These activities are linked to its divergent subcellular localization, which spreads from the plasma membrane, focal adhesions, endosomal compartments, to the early secretory pathway.

A key feature of syntenin-1 is its ability to coordinate signaling complexes via PDZ domain-mediated interactions. The PDZ tandem binds diverse partners, including Frizzled receptors [Egea-Jimenez A. L., et al., 2016], phosphatidylinositol 4,5-bisphosphate (PIP2) [Zimmermann, P., et al., 2002], and viral proteins [Jimenez-Guardeño, J. M., et al., 2014], through cooperative mechanisms that enhance binding avidity. For example, PDZ2 engages in tripartite interactions with the Frizzled 7 C-terminus and PIP2, leveraging adjacent binding pockets to stabilize membrane-associated signaling platforms [Egea-Jimenez, A. L., et al., 2016]. Such interactions underpin syntenin-1's role in non-canonical Wnt signaling and syndecan recycling, processes critical for cell polarity and growth factor responses [Luyten, T., et al., 2008].

Involvement of syntenin-1 in many important biological processes highlights syntenin-1 as a target for drug discovery. Thus, for example, atomic-resolution structures of syntenin-1's PDZ domains are critical for rational drug design. The X-ray crystal structure of PDZ1 bound to the inhibitor KSL-128018 (PDB code: 6AK2) reveals a noncanonical binding mode involving residues beyond the canonical groove, including Trp-4 and Chg-2, which engage in hydrogen bonds and hydrophobic interactions [Kang, B. S., et al., 2003]. Similarly, PDZ2's PIP2-binding pocket, adjacent to the peptide groove, is stabilized by water-mediated networks [Zimmermann, P., et al., 2002]. These structural details may explain how syntenin-1 achieves high-affinity interactions with diverse partners and highlight targetable regions for disrupting oncogenic signaling.

Accordingly, the extended binding interfaces and hydration networks between PDZ1 and PDZ2 position syntenin-1 as a promising therapeutic target. Inhibitors such as KSL-128114, designed to leverage these structural features, demonstrate nanomolar affinity, metabolic stability, and efficacy in glioblastoma models [Haugaard-Kedström et al., 2021]. Targeting syntenin-1's PDZ-mediated interactions with syndecans, Frizzled receptors, or viral proteins (e.g., SARS-CoV-2 E protein) could mitigate cancer metastasis, neurodevelopmental disorders, and viral pathogenesis, respectively [Boukerche, H., et al., 2005][Kegelman, T. P., et al., 2014] [Gordon-Alonso, M., et al., 2012]. Thus, high-resolution structural data of individual PDZ domains may further enable

109 the development of domain-selective inhibitors to modulate syntenin-1's multifunctional roles in
110 disease.

111 Initially, we aimed to resolve the drug-PDZ1 complex structure for anthranilic acid derivatives,
112 analogs of Dishevelled PDZ inhibitors [Hori, K. et al,, 2018]. While co-crystallization attempts
113 with these compounds were unsuccessful, we determined ten high-resolution apo-form crystal
114 structures of the syntenin-1 PDZ1-PDZ2 tandem including one crystal of PDZ1-PDZ2 tandem
115 complexed with compound E5 (PDZ2i) [Hoffer, L. et al., 2023]. Structural analysis revealed
116 significant conformational variation in PDZ1's canonical ligand-binding pocket, contrasting with
117 PDZ2's static architecture. Here, we evaluate conformational divergence across 20 PDZ1
118 structures from the ten independent crystals and compare them to PDZ2. GROMACS-based
119 molecular dynamics (MD) simulations of isolated PDZ1 and PDZ2 domains further highlighted
120 intrinsic flexibility in PDZ1's Lys119-Ile125 and Ala181-Glu184 loops.

121

122 **Materials and Methods**

123 *1. Expression and Purification of Protein Samples*

124 The DNA fragment encoding the human syntenin-1 PDZ tandem (residues 113-273 and 113-276,
125 see Figure 1) was amplified via polymerase chain reaction (PCR) and subsequently cloned into a
126 glutathione-S-transferase (GST)-fusion expression vector, which included an PreScission™
127 Protease (Cytiva, Tokyo, Japan) cleavage site. Protein expression was induced by the addition of
128 1 mM isopropyl β-D-1-thiogalactopyranoside (IPTG) in *Escherichia coli* BL21-CodonPlus
129 (DE3)-RIL Competent Cells ((Agilent Technologies Japan, Ltd., Tokyo, Japan). The PDZ tandem
130 was expressed in LB medium, and cell pellets were subsequently lysed by sonication. The lysate
131 was clarified through centrifugation and purified by affinity chromatography using COSMOSIL®
132 GST Accept (nacalai tesque, Inc., Kyoto, Japan) in a buffer containing 50 mM Tris-HCl (pH 7.5),
133 150 mM NaCl, and 1 mM EDTA. The GST-tagged protein was then subjected to cleavage using
134 PreScission™ Protease at 4°C. After complete digestion, the cleaved PDZ tandem was separated
135 from GST and further purified by gel filtration chromatography using HiLoad™ 26/600
136 Superdex™ 75 prep grade (Cytiva). The protein-containing elution was subsequently dialyzed in
137 a buffer composed of 25 mM HEPES (pH 7.4), 150 mM NaCl, and 1 mM DTT.

138 *2. Crystallization and Data collection*

139 Crystallization experiments were conducted using the sitting drop vapor diffusion method at 20°C.
140 The specific crystallization conditions for the apo-syntenin-1 PDZ protein are detailed below: In
141 this study, we initially intended to obtain the crystals of the complex between the PDZ tandem
142 and the anthranilic PDZ inhibitors, NPL1010, 3005, 3026, and 3027. The chemical structures of
143 the compounds are summarized in Supplementary Figure 1.

144 • **S1 (PDB code: 9VA6)**: Crystals were obtained from a solution containing 5 mM NPL3005,
145 0.2 M Sodium chloride, 0.1 M HEPES pH 7.5, and 25% w/v Polyethylene glycol (PEG) 3,350.

146 • **S2 (PDB code: 9VA9)**: Crystals were obtained from a solution containing 5 mM NPL3005,
147 0.2 M Sodium formate, and 20% w/v PEG 3,350.

148 • **S3 (PDB code: 9VAC)**: Crystals were obtained from a solution containing 5 mM
149 NPL3026, 0.2 M Ammonium acetate, 0.1 M Sodium citrate tribasic dihydrate pH 5.6, and 30%
150 w/v PEG 4,000.

151 • **S4 (PDB code: 9VAD)**: Crystals were obtained from a solution containing 5 mM
152 NPL3027, 0.2 M Lithium sulfate monohydrate, 0.1 M Tris pH 8.5, and 25% w/v PEG 3,350.

153 • **S5 (PDB code: 9VAF)**: Crystals were obtained from a solution containing 5 mM PDZ1i,
154 0.2 M Sodium chloride, 0.1 M BIS-TRIS pH 5.5, and 25% w/v PEG 3,350.

155 • **S6 (PDB code: 9VAI)**: Crystals were obtained from a solution containing 0.2 M
156 Ammonium acetate, 0.1 M Sodium acetate trihydrate pH 4.6, and 30% w/v PEG 4,000.

157 • **S7 (PDB code: 9VAL)**: Crystals were obtained from a solution containing 0.2 M Sodium
158 chloride, 0.1 M Tris pH 8.5, and 25% w/v PEG 3,350.

159 • **S8 (PDB code: 9VB9)**: Crystals were obtained from a solution containing 5 mM NPL1010,
160 0.1 M BIS-TRIS pH 5.5, and 25% w/v PEG 3,350.

161 • **S9 (PDB code: 9VBB)**: Crystals were obtained from a solution containing 5 mM
162 NPL1010, 0.2 M Ammonium acetate, 0.1 M BIS-TRIS pH 5.5, and 25% w/v PEG 3,350.

The crystallization condition for the syntenin-1 PDZ protein-compound complex is outlined below:

- **S10 (PDB code: 9V90)**: Co-crystallization was performed in a solution containing 0.5 mM PDZ2i, 0.4 M ammonium acetate, 0.1 M Sodium acetate pH 4.6, and 20% PEG 3,350.

All crystals were grown from a protein concentration of 6 mg/mL. Crystals were cryo-protected by immersion in mother liquor supplemented with 10% (v/v) glycerol before freezing. Diffraction data for syntenin-1 PDZ crystals were collected at the Photon Factory BL-17A and processed using X-ray Detector Software (XDS), [Kabsch., W. et al, 2010]. The phase problem was solved by molecular replacement using the structure of PDB code: 8BLU as a template with the program PHASER [McCoy, A. J. et al., 2007]. Models were refined using Phenix [Adams, P. D. et al., 2010]. The figures were prepared using PyMOL software (http://www.pymol.org/).

3. Molecular Dynamics

Preparation of Initial Structures.

The PDZ1 and PDZ2 domains were defined as residues 113-193 and 197-273, respectively, and extracted from the original crystallographic structure to serve as initial coordinates for MD simulations. To ensure consistent construction of simulation boxes for both PDZ1 and PDZ2 domains, the PDZ2 domain was structurally aligned to the PDZ1 domain using the "align" command in PyMOL, and this superposed model was subsequently used as the initial structure. GROMACS (version: 2024.5) [Van Der Spoel, D. et al., 2005] was employed as the MD engine, utilizing the charmm36-jul2022.ff force field, a GROMACS adaptation of charmm36 (Huang, J. et al., 2017). Throughout all simulation procedures, hydrogen atoms were constrained to their ideal geometry using the riding model, and a time step size of 2 fs was applied.

Simulation System Construction.

The initial protein structure was embedded within a dodecahedron simulation box. Prior to solvation, the system was energy-minimized in vacuum using the steepest descent algorithm for

a maximum of 500,000 iterations to eliminate any steric clashes between atoms. The minimized model was then solvated with the TIP3P water model, whose geometry was provided as spc216. To achieve a neutral net charge, the system was ionized with 0.1 M-equivalent NaCl-derived ions, and the solvated system underwent a second round of energy minimization. Finally, the system was subjected to a very short NVT simulation (1 ps at 300 K) with harmonic restraints applied to all heavy atoms to ensure the absence of any severe residual steric clashes.

Equilibration and Production Run.

A 2-fs time step was consistently used in all MD simulations. The system was equilibrated through sequential 100-ps NVT and subsequent NPT simulations at 300 K and 1 bar, with heavy-atom restraints for each trajectory. Different random seeds were used to generate initial velocities for each independent run. Five independent 200-ns production runs were performed for each of the isolated PDZ1 or PDZ2 domains. The final 160 ns of each trajectory was subsequently extracted for detailed analysis.

Fluctuation Analysis.

The root-mean-squared fluctuation (RMSF) was computed for each Cα atom from frames sampled every 100.0 ps from the final 160 ns of the 200 ns trajectories. These trajectory-averaged residue-wise RMSF values were then used to calculate their mean and standard deviation across the five independent runs.

Results and Discussion

To gain comprehensive insights into the dynamic structural changes of syntenin-1, we conducted a statistical comparison of the crystal structures obtained. As depicted in Figure 1, syntenin-1 molecules form dimeric assemblies within the crystal lattice, resulting in each asymmetric unit containing four PDZ domains (two PDZ1 and two PDZ2 domains from two chains). From a total

217 of 10 determined crystal structures, we obtained 20 structures for the PDZ1 domain and 20
218 structures for the PDZ2 domain. The PDZ1 domain encompasses residues Glu114 to Arg193
219 (colored orange), while the PDZ2 domain spans residues Arg197 to Phe273 (colored blue). The
220 apo-syntenin-1 structure was determined using a 163-amino acid construct, whereas the syntenin-
221 1-compound complex structure utilized a 166-amino acid construct. Then, comparative analysis
222 of these ten PDZ1-PDZ2 tandem structures revealed significant conformational heterogeneity
223 exclusively within the PDZ1 domain of chain B. In contrast, the PDZ1 domain of chain A and
224 both PDZ2 domains (chains A and B) exhibited structural conservation, as evidenced by
225 superimposition analyses (Figures 2A, B, D, E). To quantify this observed divergence, we
226 conducted statistical evaluations of root-mean-square deviation (RMSD) of backbone Ca
227 positions. Initially, we classified these crystal structures based on their structural similarity.
228 Pairwise RMSD values were computed for all possible pairs derived from the 20 PDZ1 as well
229 as 20 PDZ2 domain structures. The resulting two-dimensional data matrix of pairwise RMSD was
230 subjected to hierarchical clustering in both rows and columns. The data were sorted by closely
231 related structural clusters in proximity. A heatmap was then generated, with color-coding
232 indicating the level of pairwise RMSD (Figure 3).

233

234 For the PDZ1 domain, major clusters were observed to form between chain A/chain B pairs
235 (Figure 3A). It should be noted that the dominant structural difference between chain A and chain
236 B probably arises from crystal packing contacts. We concluded that the overall structural
237 difference observed between PDZ1_chain_A and PDZ1_chain_B DO NOT reflect the
238 intrinsically dynamic nature of PDZ1. In contrast, relatively large structural fluctuations were
239 observed within PDZ1 domains of chain B/chain B pairs, suggesting that the intrinsic structural
240 flexibility of the syntenin-1 PDZ1 domain becomes apparent in this context. Among this cluster,
241 however, apo6 and apo7, which were crystallized without compounds, fell into the same structural
242 subcluster, apart from the other subclusters that were crystallized with NPL inhibitors. Thus, we
243 could not rule out that presence of inhibitors in crystallizing conditions exert some influence on
244 structural differences of PDZ1. Conversely, PDZ1 of chain A/chain A pairs did not exhibit
245 remarkable pairwise RMSD values, indicating generally similar structures across these instances
246 (Figure 3A). Notably, the presence or absence of a compound in the crystallization condition did

247 not influence the clustering of chain A/chain A pairs. This suggests that small structural diversity
248 was primarily due to the restrictions imposed by crystal contacts and not affected by presence of
249 absence of the PDZ inhibitors.

250

251 Next, we analyzed the structural differences of PDZ2 domains, which also exhibited two
252 dominant clusters based on the difference between chain A and chain B (Figure 3B). However,
253 unlike PDZ1, the hierarchical clustering analysis of PDZ2 structure succeeded in separating
254 structures of apo3_chain A and both chain A and chain B of the complex structures into distinct
255 major clusters. This result can be explained by the binding of the inhibitor PDZ2i, which may fix
256 the loop conformation. However, interestingly, we observed that the apo3_chain A structure is
257 very similar to that of the complex structures. Thus, we expected that "conformational selection"
258 mechanism may work rather than "induced fit" upon PDZ2i binding to PDZ2 of syntehin-1.
259 Accordingly, when comparing the structural differences among PDZ1 and PDZ2, PDZ1
260 consistently exhibited higher pairwise RMSD values than PDZ2. This observation strongly led us
261 to hypothesize that PDZ1 possesses greater structural flexibility than PDZ2.

262

263 Accordingly, we visualized the selected pairs of PDZ domains and structural clusters by
264 superimposing (Figure 2). The pair apo2_chainB_PDZ1/apo9_chainB_PDZ1 displayed the
265 largest pairwise RMSD value among all PDZ1 pairs (Figure 2C). The PDZ1 domain demonstrated
266 diverse structures in the loops surrounding the canonical ligand binding pocket. As mentioned
267 previously, greater structural polymorphism was consistently observed in PDZ1 domains of chain
268 B compared to those of chain A, when all obtained PDZ1 structures within chain A and chain B
269 had compared each other, respectively (Figure 2A, 2B). In contrast, comparisons of PDZ2
270 domains within both chain A and chain B (Figure 2D, E) revealed no significant structural
271 polymorphism, suggesting a rigid structure for PDZ2. Furthermore, a comparison between the
272 bound and unbound structures of the PDZ2 domain (Figure 2F) exhibited only a small structural
273 difference in a loop region analogous to where polymorphism was observed in the PDZ1 domain.

274

275 To analyze this structural diversity in detail, we calculated the RMSD for each residue within the
276 syntenin-1 PDZ domains. For all PDZ domain pairs depicted in Figure 2, the pairwise RMSD for
277 each residue was calculated, and their average values were plotted against the residue numbers
278 (Figure 4). For PDZ1, locally high average pairwise RMSD values were observed in the Lys119-
279 Ile125 loop and the Ala181-Glu184 loop, which are surrounding the canonical ligand binding
280 pocket (Figure 4A). This suggests that these regions are intrinsically flexible. Additionally, minor
281 peaks were observed at Ala143 and Leu149. In contrast, for PDZ2, although peaks were present
282 in the aforementioned loops, they did not exhibit the same high average pairwise RMSD values
283 observed for PDZ1 (Figure 4B). Small peaks were also observed at Asp224 and Gly243. Overall,
284 the crystal structure analysis clearly indicated that PDZ1 exhibits higher structural flexibility than
285 PDZ2, particularly in the identified loop regions.

286

287 The structural heterogeneity observed in PDZ1 loop regions across ten crystallographic datasets
288 prompted the hypothesis that these loops exhibit inherent conformational flexibility in solution, a
289 property potentially linked to syntenin-1's multifunctional role in cellular processes. To evaluate this
290 hypothesis, we conducted molecular dynamics (MD) simulations of isolated human syntenin-1 PDZ
291 domains using the GROMACS software package (Figure 5). Comparative analysis revealed enhanced
292 flexibility in PDZ1 loop regions relative to PDZ2, consistent with crystallographic observations.
293 Strikingly, simulations identified two previously uncharacterized regions of elevated mobility: (region
294 i) residues Ile132-Gly135 in PDZ1 and (region ii) residues Asn230-Leu232 in PDZ2. Both regions are
295 localized to the PDZ1-PDZ2 interdomain interface (Figure 6), with >80% of constituent residues
296 participating in interdomain contacts. In detail, mainchain and side chain of Asp133 in region i of
297 PDZ1 formed hydrogen bonds with Thr234 in PDZ2 (Figure 6A). Similarly, Gly231 in region ii
298 in PDZ2 formed a hydrogen bond with Gln157 PDZ1 (Figure 6B). Thus, these regions may have
299 additional intrinsic flexibility, although they adopted rather fixed conformations in tandem PDZ1-
300 PDZ2 domain architecture of human syntenin-1.

301

302 **Conclusion**

This study provides compelling evidence that PDZ1 in human Syntenin-1 exhibits inherent conformational diversity compared to PDZ2's rigid architecture, despite their sequential similarity. Through extensive crystallographic analysis and molecular dynamics simulations, we demonstrate that PDZ1's structural plasticity is concentrated in key ligand-binding loops, suggesting a conformational selection mechanism for diverse partner recognition. In contrast, PDZ2 maintains remarkable structural conservation, indicating distinct evolutionary constraints on these tandem domains. The observed dynamic asymmetry explains Syntenin-1's versatility in cellular signaling pathways and offers a rational foundation for developing domain-selective inhibitors targeting cancer metastasis, viral pathogenesis, and neurodevelopmental disorders. Our findings highlight the importance of multi-structure comparisons and hierarchical analysis for accurately mapping protein dynamic landscapes, beyond what B-factors alone can reveal.

Conflict of Interest

Among the authors, T.T. and H.H. are the founders of a Nagoya University-based spinoff startup company, called BeCellBar. LLC. The remaining authors declare no conflicts of interest.

Author Contributions

Conceptualization, T.T., N.I., and H.H.; Investigation, N.A., Y.H., K.S., N.N. and T.T.; Graphics, Table and Charts, N.A. and K.S.; Data Analysis, N.A., Y.H., K.S., N.N. and T.T.; Resources, Y.H., K.S., N.N., T.T.; Writing and Original Draft Preparation, N.A. and H.H.; Writing, Reviewing and Editing, N.I. and H.H.; Supervision, N.I. and H.H.; Project Administration, H.H.; Funding Acquisition, H.H. All authors have read and agreed to the published version of the manuscript.

Funding

This study was supported by Nanken-Kyoten, TMDU. This study was also supported by JSPS KAKENHI Grant Number [24K0214524] (Grant-in-Aid for Scientific Research (B)) to H.H., AMED Program for Innovative Drug and Medical Device Development against Emerging and

Re-emerging Infectious Diseases (22fk0108527) to H.H, and Astellas Foundation for Research on Metabolic Diseases (FY2021, COVID-19 Special Grant) to H.H.

Acknowledgments

The synchrotron radiation experiments were performed with the approval of the Photon Factory Program Advisory Committee (Proposal No. 2022G024, No. 2024G043).

Data Availability Statement

The datasets of crystallographic analyses are deposited to the Protein Data Bank. Other related data (MD trajectories) will be available at the request to authors.

References

Adams, P. D., Afonine, P. V, Bunkóczi, G., Chen, V. B., Davis, I. W., Echols, N., et al. (2010). PHENIX: A comprehensive Python-based system for macromolecular structure solution. Acta Crystallogr D Biol Crystallogr 66, 213–221.

Baietti, M. F., Zhang, Z., Mortier, E., Melchior, A., Degeest, G., Geeraerts, A., et al. (2012) Syndecan-syntenin-ALIX regulates the biogenesis of exosomes. Nat Cell Biol 14, 677-685.

Boukerche, H., Su, Z., Prévot, C., Sarkar, D., Fisher, P. B. (2008). mda-9/Syntenin promotes metastasis in human melanoma cells by activating c-Src. Proc Natl Acad Sci U S A 105, 15914-15919.

Egea-Jimenez, A. L., Gallardo, R., Garcia-Pino, A., Ivarsson, Y., Wawrzyniak, A. M., Kashyap, R., et al. (2016) Frizzled 7 and PIP2 binding by syntenin PDZ2 domain supports Frizzled 7 trafficking and signalling. Nat Commun. 7, 12101.

Gordón-Alonso M, Rocha-Perugini V, Álvarez S, Moreno-Gonzalo O, Ursa A, López-Martín S, et al. (2012) The PDZ-adaptor protein syntenin-1 regulates HIV-1 entry. Mol Biol Cell. 12, 2253-2263.

Grootjans, J. J., Zimmermann, P., Reekmans, G., Smets, A., Degeest, G., Dürr, J., et al. (1997) Syntenin, a PDZ protein that binds syndecan cytoplasmic domains. Proc Natl Acad Sci U S A. 94, 13683-13688.

Haugaard-Kedström, L. M., Clemmensen, L. S., Sereikaite, V., Jin, Z., Fernandes, E. F. A., Wind, B., et al., (2021) A High-Affinity Peptide Ligand Targeting Syntenin Inhibits Glioblastoma. J Med Chem. 64, 1423-1434.

Hirbec, H., Martin, S., Henley, J. M. (2005) Syntenin is involved in the developmental regulation of neuronal membrane architecture. Mol. Cell. Neurosci. 4, 737-746.

Hoffer, L., Garcia, M., Leblanc, R., Feracci, M., Betzi, S., Yaala, K. B., et al. (2023) Discovery of a PDZ Domain Inhibitor Targeting the Syndecan/Syntenin Protein-Protein Interaction: A Semi-Automated "Hit Identification-to-Optimization" Approach. J. Med. Chem, 66, 4633-4658.

Hori, K., Ajioka, K., Goda, N., Shindo, A., Takagishi, M., Tenno, T., et al. (2018) Discovery of Potent Disheveled/Dvl Inhibitors Using Virtual Screening Optimized With NMR-Based Docking Performance Index. Front Pharmacol. 9, 983.

Huang, J., Rauscher, S., Nawrocki, G., Ran, T., Feig, M., de Groot B. L., et al. (2017) CHARMM36m: An improved force field for folded and intrinsically disordered proteins. Nat Methods. 1, 71–73.

Jimenez-Guardeño, J. M., Nieto-Torres, J. L., DeDiego, M. L., Regla-Nava, J. A., Fernandez-Delgado, R., Castaño-Rodriguez, C., et al. (2014) The PDZ-binding motif of severe acute respiratory syndrome coronavirus envelope protein is a determinant of viral pathogenesis. PLoS Pathog. 10, e1004320.

Kabsch, W. (2010) XDS. Acta Crystallogr D Biol Crystallogr. 66, 125-132.

Kang, B. S., Cooper, D. R., Jelen, F., Devedjiev, Y., Derewenda, U., Dauter, Z., et al. (2003) PDZ tandem of human syntenin: Crystal structure and functional properties. Structure. 4, 459-468.

380 Kegelman, T. P., Das, S. K., Hu, B., Bacolod, M. D., Fuller, C. E., Menezes, M. E., et al. (2014)
381 MDA-9/Syntenin is a key regulator of glioma pathogenesis. Neuro Oncol. 1, 50-61.

382 Luyten, T., Mortier, E., Van Campenhout, C., Taelman, V., Degeest, G., Wuytens, G., et al. (2008)
383 The postsynaptic density 95/disc-large/zona occludens protein syntenin directly interacts with
384 Frizzled 7 and supports noncanonical Wnt signaling. Mol Biol Cell. 4, 1594-1604.

385 McCoy, A. J., Grosse-Kunstleve, R. W., Adams, P. D., Winn, M. D., Storoni, L. C., Read, R. J.
386 (2007) Phaser crystallographic software. J Appl Crystallogr. 40, 658–674.

387 Van Der Spoel, D., Lindahl, E., Hess, B., Groenhof, G., Mark, A. E., Berendsen, H. J. (2005)
388 GROMACS: Fast, Flexible, and Free. J Comput Chem 26, 1701-1718.

389 Zimmermann, P., Tomatis, D., Rosas, M., Grootjans, J., Leenaerts, I., Degeest, G., et al. (2001)
390 Characterization of syntenin, a syndecan-binding PDZ protein, as a component of cell adhesion
391 sites and microfilaments. Mol Biol Cell. 2, 339-350.

392 Zimmermann, P., Meerschaert, K., Reekmans, G., Leenaerts, I., Small, J. V., Vandekerckhove, J.,
393 et al. (2002) PIP_2-PDZ domain binding controls the association of syntenin with the plasma
394 membrane. Mol Cell. 6 1215-1225.

395 Zimmermann, P., Zhang, Z., Degeest, G., Mortier, E., Leenaerts, I., Coomans, C., et al. (2005)
396 Syndecan recycling is controlled by syntenin-PIP_2 interaction and Arf6. Dev Cell. 9, 377-388.

397

398

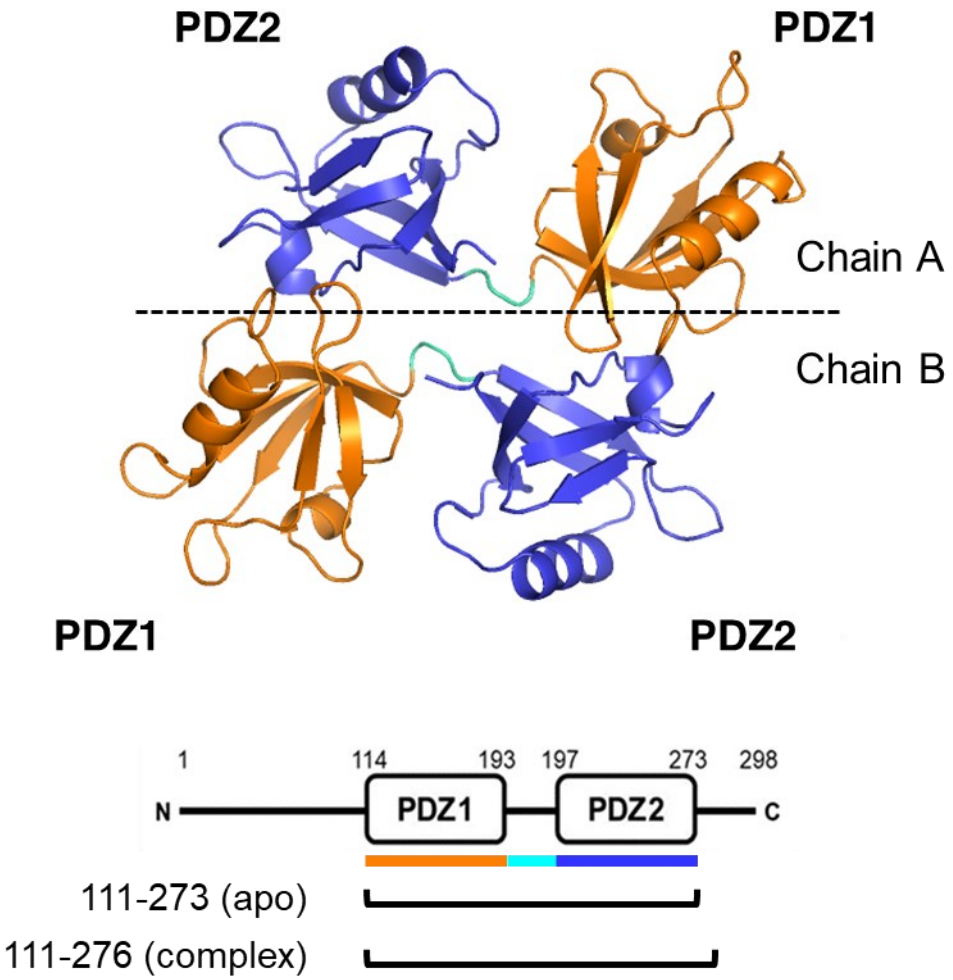

Figure 1:

Crystal structure and domain structure of the apo-syntenin-1. The crystal structure contains two molecules of the syntenin-1. The PDZ1 domain is assigned Glu114 to Arg193 (orange), and the PDZ2 domain is assigned Arg197 to Phe273 (blue). 163 amino acids construct was used to determine the structure of apo-syntenin-1. 166 amino acids construct was used to determine the structure of syntenin-1-compound complex.

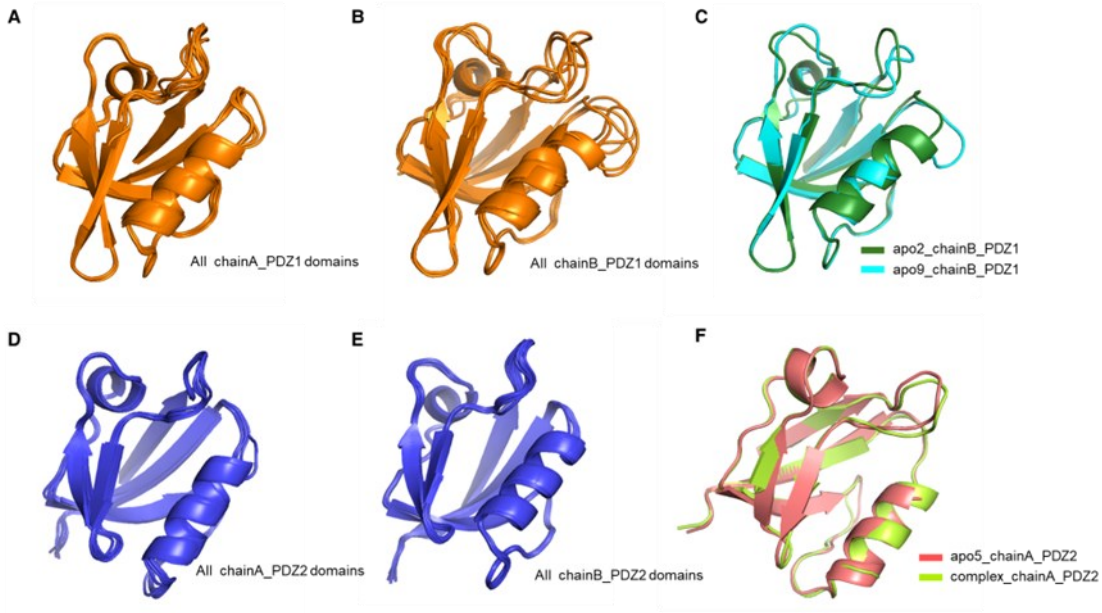

Figure 2:

Comparison by superposition between each PDZ domain. A: Comparison of all nine structures of the apo PDZ1 domain of chain A. B: Comparison of all nine structures of the apo PDZ1 domain of chain B. C: Comparison of the pairs with highest pairwise RMSD among PDZ1 domain of chain B. D: Comparison of all nine structures of the apo PDZ2 domain of chain A. E: Comparison of all nine structures of the apo PDZ2 domain of chain B. F: Comparison of the bound and unbound structures of the PDZ2 domain.

A

PDZ1

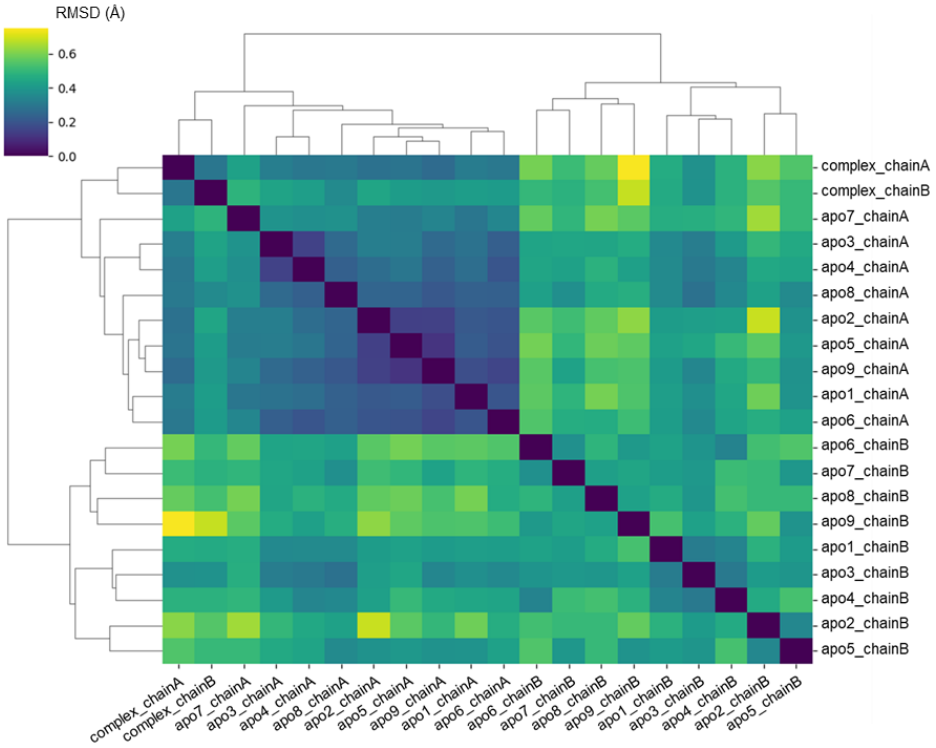
RMSD (Å)
0.6
0.4
0.2
0.0
complex_chainA
complex_chainB
apo7_chainA
apo3_chainA
apo4_chainA
apo8_chainA
apo2_chainA
apo5_chainA
apo9_chainA
apo1_chainA
apo6_chainA
apo6_chainB
apo7_chainB
apo8_chainB
apo9_chainB
apo1_chainB
apo3_chainB
apo4_chainB
apo2_chainB
apo5_chainB

B

PDZ2

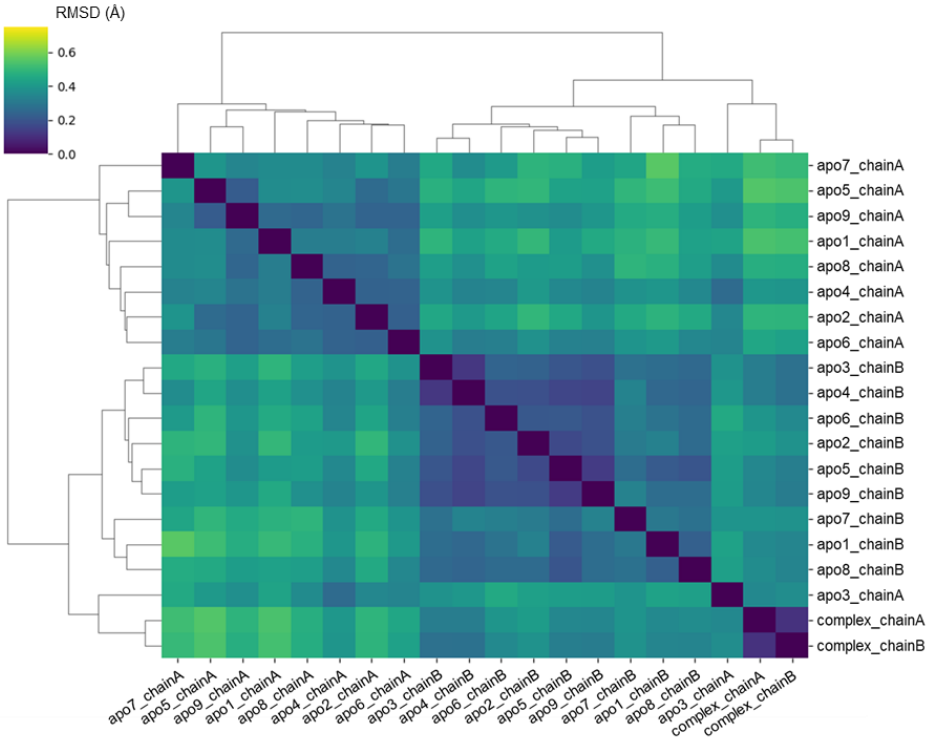
RMSD (Å)
0.6
0.4
0.2
0.0
apo7_chainA
apo5_chainA
apo9_chainA
apo1_chainA
apo8_chainA
apo4_chainA
apo2_chainA
apo6_chainA
apo3_chainB
apo4_chainB
apo6_chainB
apo2_chainB
apo5_chainB
apo9_chainB
apo7_chainB
apo1_chainB
apo8_chainB
apo3_chainA
complex_chainA
complex_chainB

419 Figure 3:

420 Cluster analysis of syntenin-1 PDZ domains. The structures of PDZ domains were extracted one
421 by one from 9 apo structures and 1 complex structure, and the structures of 20 PDZ domains were
422 obtained respectively. Pairwise RMSD was calculated for all pairs produced from 20 PDZ
423 domains. Pairwise RMSD levels were classified from yellow to dark blue, and the similarity
424 between each pair was represented in a heatmap. Based on the similarity, the cluster analysis was
425 performed, and the results were expressed in a cluster dendrogram. A: Cluster analysis of PDZ1
426 domains. Major clusters were formed in chain A and chain B, respectively. B: Cluster analysis of
427 PDZ2 domains. Major clusters were formed in apo chain A and apo chain B. A minor cluster was
428 formed by apo3 chain A and complex structures.

429

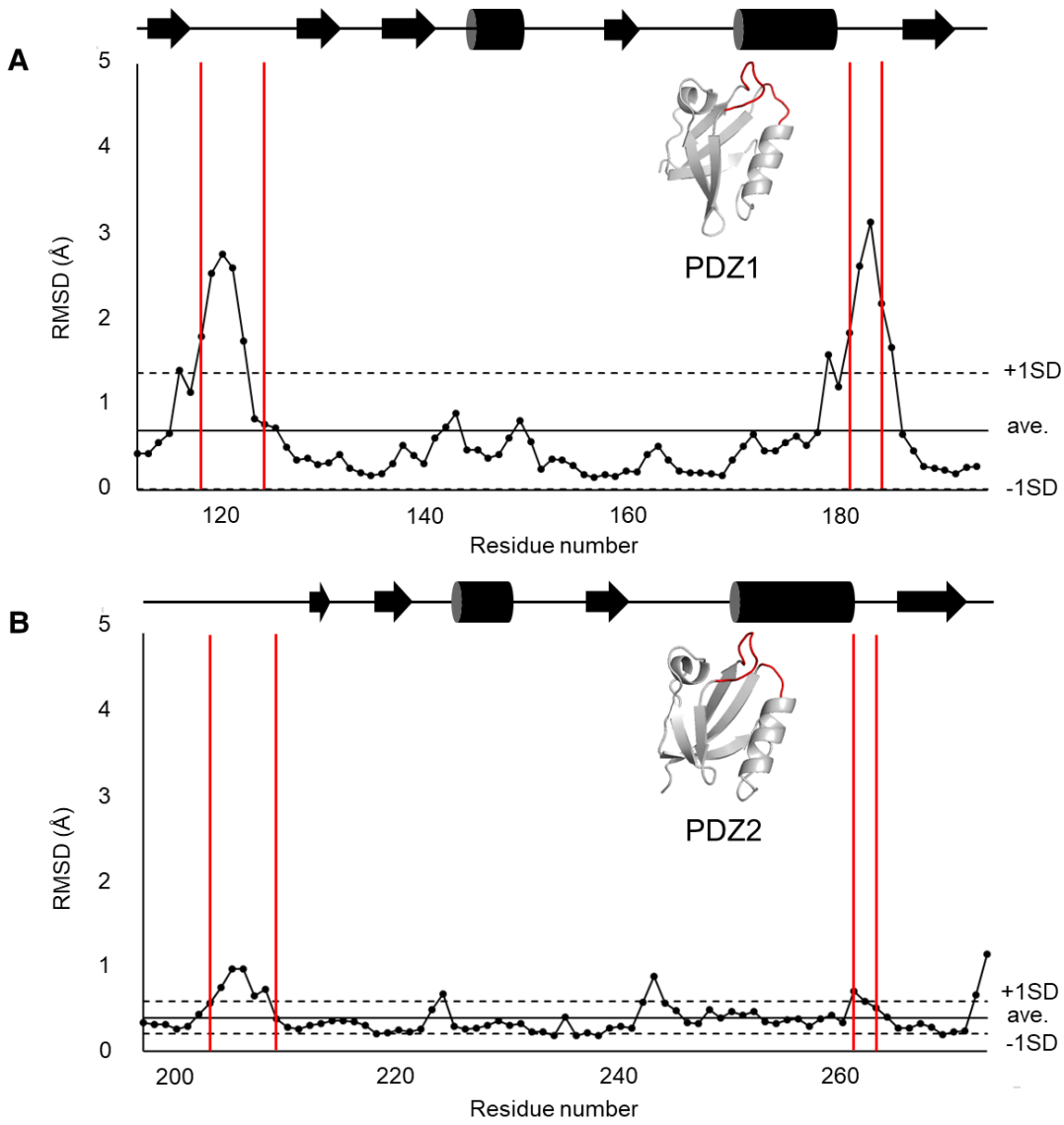

Figure 4:

Average pairwise RMSD for each residue calculated by comparison of crystal structures. Highlighted areas (red) are the sites of molecular fluctuations in the PDZ1 domain. A: Average pairwise RMSD for each residue in the PDZ1 domain. B: Average pairwise RMSD for each residue in the PDZ2 domain. The diagrams of the secondary structures were shown in the top of the panels.

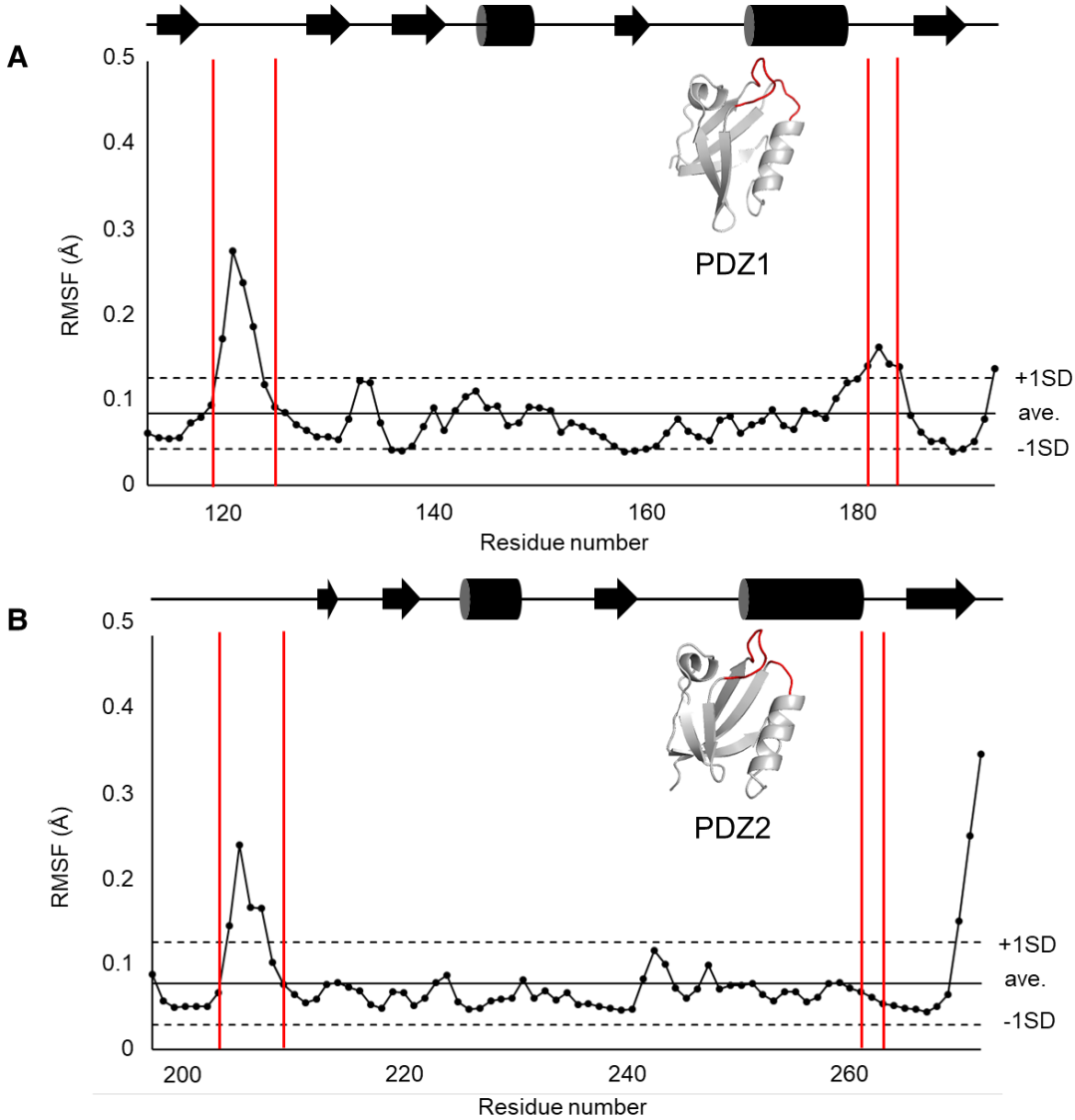

Figure 5:

RMSF for each residue calculated by MD calculations. Highlighted areas show molecular fluctuations in the PDZ1 domain. A: RMSF for each residue in the PDZ1 domain. B: RMSF for each residue in the PDZ2 domain. The diagrams of the secondary structures were shown in the top of the panels.

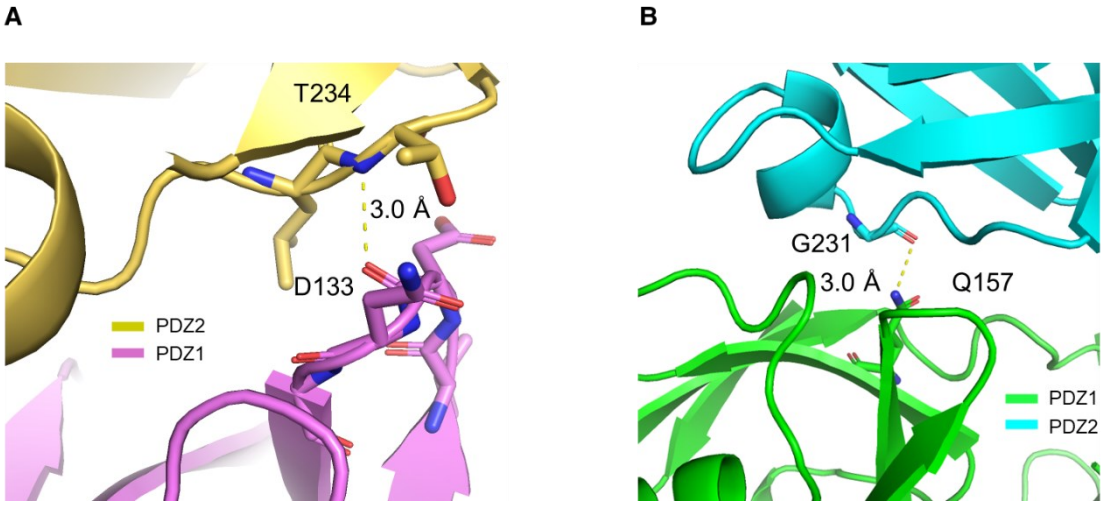

Figure 6:

The residues that exhibited a high RMSF in MD simulations with a low structural diversity in the ten crystal structures. A: Around Ile132 to Gly135 in PDZ1. B: Around Asn230 to Leu232 in PDZ2.